

# Operando Observation of Chemical Transformations of Iridium Oxide During Photoelectrochemical Water Oxidation

Lin Li<sup>1,2\*</sup>, Jinhui Yang<sup>3‡</sup>, Harri Ali-Löytty<sup>1,4</sup>, Tsu-Chien Weng<sup>5</sup>, Francesca M. Toma<sup>3</sup>, Dimosthenis Sokaras<sup>5</sup>, Ian D. Sharp<sup>3,6\*</sup>, and Anders Nilsson<sup>1\*</sup>

<sup>1</sup> SUNCAT Center for Interface Science and Catalysis, SLAC National Accelerator Laboratory, 2575 Sand Hill Road, Menlo Park, CA 94025, USA.

<sup>2</sup> Department of Chemistry - Ångström Laboratory, Uppsala University, 751 20 Uppsala, Sweden.

<sup>3</sup> Joint Center for Artificial Photosynthesis, Lawrence Berkeley National Laboratory, 1 Cyclotron Road, Berkeley, CA 94720, USA.

<sup>4</sup> Surface Science Laboratory, Optoelectronics Research Centre, Tampere University of Technology, FI-33101 Tampere, Finland.

<sup>5</sup> Stanford Synchrotron Radiation Light Source, SLAC National Accelerator Laboratory, 2575 Sand Hill Road, Menlo Park, CA 94025, USA.

<sup>6</sup> Walter Schottky Institut and Physik Department, Technische Universität München, Am Coulpmbwall 4, 85748 Garching, Germany

‡Equal contribution, Lin Li and Jinhui Yang contributed equally to this work

\* E-mail: [lin.li@kemi.uu.se](mailto:lin.li@kemi.uu.se), [sharp@wsi.tum.de](mailto:sharp@wsi.tum.de), [nilsson@slac.stanford.edu](mailto:nilsson@slac.stanford.edu)

**KEYWORDS.** *Operando method, high energy resolution fluorescence detection X-ray absorption spectroscopy (HERFD XAS), iridium oxide, electrochemical and photoelectrochemical (PEC), oxygen evolution reaction (OER).*

**ABSTRACT:** Iridium oxide is one of the few catalysts capable of catalyzing the oxygen evolution reaction (OER) in both acidic and basic conditions. Understanding the mechanism of IrO<sub>x</sub> under realistic photoelectrochemical conditions is important for the development of integrated water splitting systems. Herein, we have developed a highly efficient OER photoanode in pH 1 aqueous solutions based on a sputtered IrO<sub>x</sub> film and a p+n-Si light absorber, interfaced with sputtered Au layer. *Operando* high energy resolution fluorescence detection X-ray absorption spectroscopy (HERFD XAS) was employed to monitor the oxidation state changes of IrO<sub>x</sub> during both electrochemical and photoelectrochemical (PEC) water oxidation reactions in pH 1 aqueous solutions. We observed a gradual increase of the average oxidation state of Ir with increasing anodic potential in the pre-catalytic region, followed by a reduction of Ir under O<sub>2</sub> evolution conditions. Consistent results were obtained on dark anodes and illuminated photoanodes. However, when the thickness of IrO<sub>2</sub> was increased to 2 and 3 nm, the spectral changes became much less pronounced and the reduction of Ir oxidation state after the OER onset was not observed. This is due to the lower surface to bulk ratio, where lattice oxygen sites in the bulk are not accessible for the formation of hydroxide. More generally, the *operando* method developed here can be extended to other materials, thereby providing a powerful tool for mechanism discovery and an enabling capability for catalyst design.

Artificial photosynthesis, also referred to as solar fuels generation, provides an attractive approach to the chemical storage of solar energy as fuels, including as hydrogen generated from water.<sup>1</sup> A general approach for artificial photosynthesis is to use catalysts interfaced with light-harvesting semiconductors as photoelectrodes in photoelectrochemical (PEC) cells.<sup>2</sup> Silicon is a promising candidate as the photoelectrode due to its earth-abundance and efficient light-harvesting properties. However, the intrinsic instability of silicon in aqueous solution largely hinders its application in artificial photosynthesis. There has been significant progress in improving the stability of chemically sensitive

photoanodes, especially under extreme pH conditions. A variety of approaches, including introduction of passive or active catalytic corrosion protection layers, have been demonstrated.<sup>3–11</sup> However, for the oxygen evolution reaction, the majority of these have focused on alkaline conditions due to the narrower range of catalysts for acidic conditions.

Iridium oxide (IrO<sub>x</sub>) is one of the rarely known materials that show both high OER catalytic activity and sufficient stability in acidic conditions.<sup>12–14</sup> The chemical transformation of IrO<sub>x</sub> has been studied both *ex situ* and *in situ* under electrochemical environments, mostly on model catalysts. For example, IrO<sub>x</sub> electrocatalysts for the

OER have been investigated with synchrotron based X-ray absorption spectroscopy (XAS),<sup>15-16</sup> X-ray photoelectron spectroscopy (XPS),<sup>17</sup> and other techniques.<sup>16, 18-21</sup> XAS at the Ir L<sub>III</sub>-edge is a hard X-ray technique particularly suited for monitoring electronic structure changes under *operando* conditions, which provides information through X-ray absorption near edge structure (XANES) and extended X-ray absorption fine structure (EXAFS). The former, probed at the Ir L<sub>III</sub>-edge, provides direct information on the unoccupied Ir 5d partial density of states. In particular, the Ir 2p-5d dipole excitation gives rise to a “white-line” absorption peak in the Ir L<sub>III</sub>-edge spectrum, which can provide local information regarding the chemical state. For example, 40 nm thick anodic iridium oxide films were studied by XANES in 1 M H<sub>2</sub>SO<sub>4</sub> by Huppaufl and Lengeler.<sup>15</sup> It was found that the Ir valence varied between 3 and 4.8 over the voltammetric region of approximately -0.24 V to +1.2 V vs. Ag/AgCl.<sup>15</sup> In other work, electrodeposited iridium oxide films were examined in pH 7.3 and pH 10.7 buffer by Hillman *et al.* They proposed a two-site model and the average Ir valence change from 3.5 to 4.5 across the entire process.<sup>22</sup> A similar behavior was recently observed using electrodeposited iridium oxide films investigated in 0.5 M H<sub>2</sub>SO<sub>4</sub> by Minguzzi *et al.* and they proposed the co-existence of Ir(III) and Ir(V) under OER conditions.<sup>23</sup> However, sputtered iridium oxide films that were 21 nm and 59 nm thick, investigated in 1 M H<sub>2</sub>SO<sub>4</sub> by Pauporte *et al.* showed different characteristics. They observed that the Ir valence only increased from 3 to 3.85 when the potential was increased from -0.24 V to +1 V vs. SCE (saturated calomel electrode).<sup>24</sup> This discrepancy hints that strongly hydrated films, such as those formed via electrodeposition, exhibit fundamentally different behavior under catalytic conditions than relatively compact films formed via sputtering.

The apparent inconsistencies regarding Ir valence changes could have a number of possible origins. First, the short lifetime of the Ir 2p core-hole sets a rather broad energy resolution for conventional XAS (>5 eV), which limits the experimental sensitivity to reliably identify small spectral changes or energy shifts.<sup>25</sup> Second, as mentioned above, the iridium oxide films made from different methods may have intrinsically different characteristics, which are additionally complicated when analyzed under applied bias and in different pH solutions. Third, and finally, appropriate experimental setups for *operando* measurements are challenging to realize but are required to obtain reliable results.

Most of these *operando* studies of IrO<sub>x</sub> catalysis were directed at elucidating mechanisms and, therefore, were applied to model systems. However, it is also important to recognize that solar fuels devices often require these catalysts to be integrated onto semiconductor light absorbers and for the interfaces between the catalyst and semiconductor to be engineered to ensure stability of the complete assembly, efficient charge transport through the interface, and minimal parasitic light absorption in the catalyst.<sup>26</sup> All of this must be accomplished without

sacrificing catalytic activity. Since these engineered systems comprise significantly more complexity than the model system counterparts, it is essential to characterize realistic photoelectrodes.<sup>27-30</sup> Furthermore, an efficient catalyst needs to be thin enough to avoid parasitic light absorption, and compact enough to protect the chemically sensitive semiconductors against chemical and photochemical corrosion for PEC applications.<sup>5</sup> Therefore, the thick and porous electrocatalytically active films that have been investigated to date are not compatible with many PEC systems, and the catalytic behavior may not be transferable to the surface behavior of realistic catalysts for photoanodes. Using a realistically working photoanode to directly investigate the OER mechanism under PEC conditions is challenging,<sup>24,31</sup> but critical for achieving relevant insights and advancing the development of efficient integrated PEC systems.

Compared to conventional XAS, high energy resolution fluorescence detection XAS (HERFD XAS), in which an energetically narrow portion (~1 eV) of a selected fluorescence line is monitored, results in significantly improved resolution of X-ray absorption spectra.<sup>25, 32</sup> Furthermore, the high energy resolution of the detected x-rays limits any influence of the strong elastic and Compton scattering background signal from the electrolyte, which is typically one order of magnitude higher than the fluorescence signal of the metallic species of interest.<sup>33</sup> This advantage allows the study of ultrathin catalyst (down to sub mono-layer structures) despite the presence of electrolyte within an electrochemical cell.<sup>33</sup> We have shown that *operando* electrochemical HERFD XAS provides a unique sensitivity to the structure and chemical bonding at the Pt-electrolyte interface,<sup>34-37</sup> and allows monitoring of electronic structure changes in earth-abundant 3d transition metal catalysts for the OER.<sup>38-39</sup>

A sputter-deposited Ir/IrO<sub>x</sub> film stack on p<sup>+</sup>n-Si, where the interfacial Ir served as a protection layer for chemically sensitive Si and IrO<sub>x</sub> acted as the catalyst, was previously reported and exhibited efficient water oxidation in acidic media (1 M H<sub>2</sub>SO<sub>4</sub>).<sup>9</sup> This work inspired us to directly investigate the oxygen evolution reaction (OER) mechanism on sputtered IrO<sub>2</sub> film on p<sup>+</sup>n-Si using the *operando* XAS technique. Here, considering the local interaction between Au and metal oxides,<sup>40-41</sup> we explore the Au as an interfacial layer between the IrO<sub>x</sub> catalyst and the Si photoanode, i.e., photoelectrodes comprise IrO<sub>x</sub>/Au/p<sup>+</sup>n-Si and dark electrodes comprise IrO<sub>x</sub>/Au/p<sup>+</sup>-Si. The thickness of the ultrathin (1-3 nm) but robust IrO<sub>x</sub> was optimized and studied by *operando* Ir-L<sub>III</sub> HERFD XAS in 1 M H<sub>2</sub>SO<sub>4</sub> solution, under simulated air mass (AM) 1.5 illumination and dark conditions, respectively, thereby allowing us to access the chemical state information exclusively on the ultrathin IrO<sub>2</sub> layer during the OER reactions.

## Results and discussion

### 1. Physical and electrochemical properties of IrO<sub>2</sub>/Au/Si versus IrO<sub>2</sub>/Ir/Si.

Figure 1 (a) shows a comparison of cyclic voltammograms (CVs) from  $\text{IrO}_2/\text{Au}/\text{p}^+\text{-Si}$  photoanodes versus  $\text{IrO}_2/\text{Ir}/\text{p}^+\text{-Si}$  photoanodes under simulated AM 1.5 irradiation at  $100 \text{ mW}/\text{cm}^2$ . Also shown in Figure 1(a) are the same catalyst layers applied to degenerately doped  $\text{p}^+\text{-Si}$  ( $0.001\text{--}0.005 \Omega \text{ cm}^{-1}$ , denoted as  $\text{p}^+\text{-Si}$ ) in the dark. All CVs were acquired in  $1.0 \text{ M H}_2\text{SO}_4$ . In all cases, the nominal thickness of  $\text{IrO}_2$  was 4 nm, as determined by a quartz crystal monitor in the sputtering system. This layer thickness was selected to provide adequate catalytic activity while keeping parasitic light absorption low, as well as to enable comparisons with previously reported data.<sup>9</sup> Comparing the photoanode to the dark electrode, the onset potential, defined at the potential required to achieve a current of  $1 \text{ mA}/\text{cm}^2$ , was found to shift by  $\sim 490 \text{ mV}$  in the cathodic direction, from  $1.63 \text{ V}$  vs. RHE for  $\text{IrO}_x/\text{Ir}/\text{p}^+\text{-Si}$  in darkness to  $1.12 \text{ V}$  vs. RHE for  $\text{IrO}_x/\text{Ir}/\text{p}^+\text{-Si}$  under illumination. The onset potential and photovoltage, though not fully optimized, are comparable to the previously reported results.<sup>9</sup> When an interfacial Au layer was used instead of Ir, the onset potentials for both the dark electrode and photoanode under illumination exhibited favorable cathodic shifts of approximately  $100 \text{ mV}$ , with values of  $1.54 \text{ V}$  vs. RHE for  $\text{IrO}_x/\text{Au}/\text{p}^+\text{-Si}$  and  $1.04 \text{ V}$  vs. RHE for  $\text{IrO}_x/\text{Au}/\text{p}^+\text{-Si}$ , which yields a photovoltage of  $500 \text{ mV}$ . Comparing the Au interfacial layer to the Ir interfacial layer, the photocurrent density at  $1.23 \text{ V}$  vs RHE increased from  $5$  to  $13 \text{ mA cm}^{-2}$  and the saturation current density increased from  $13$  to  $18 \text{ mA cm}^{-2}$  for the  $\text{IrO}_x/\text{Ir}/\text{p}^+\text{-Si}$  and  $\text{IrO}_x/\text{Au}/\text{p}^+\text{-Si}$ , respectively. A similar increase of current density at a given applied electrochemical potential was observed for the catalysts deposited on  $\text{p}^+\text{-Si}$ . These results indicate that the Au interfacial layer yields better performance than the Ir interfacial layer for both EC and PEC on Si. To reveal the reason of this improvement, the physical properties of these two types of electrodes were characterized, as discussed below.

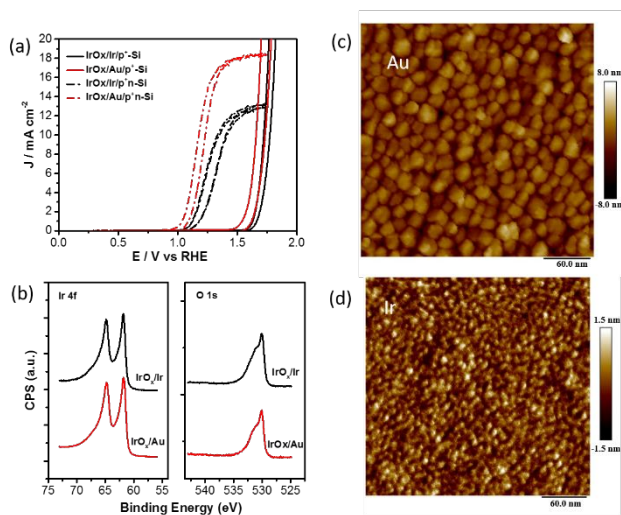


Figure 1. (a) Cyclic voltammograms for  $\text{IrO}_2/\text{Ir}/\text{Si}$  (black) and  $\text{IrO}_2/\text{Au}/\text{Si}$  (red) dark electrodes (dashed lines) and photoelectrodes (solid lines) operated in  $1 \text{ M H}_2\text{SO}_4$ , (b) X-ray photoelectron spectra of the Ir 4f and O 1s core levels from

$\text{IrO}_2/\text{Ir}/\text{Si}$  (black) and  $\text{IrO}_2/\text{Au}/\text{Si}$  (red), and (c,d) atomic force micrographs for  $\text{IrO}_2/\text{Au}/\text{Si}$  (c) and  $\text{IrO}_2/\text{Ir}/\text{Si}$  (d).

Chemical analysis via X-ray photoelectron spectroscopy (XPS) was performed to determine whether differences in composition between  $\text{IrO}_x$  deposited on Ir and on Au are present. Ir 4f and O 1s core level regions are shown in Figure 1(b), reveal that the compositions of  $\text{IrO}_x$  in the two types of samples are very similar. In particular, despite different interfacial layers, both comprise  $\text{IrO}_2$ , with binding energies of Ir 4f<sub>7/2</sub> and Ir 4f<sub>5/2</sub> at  $61.9 \text{ eV}$  and  $63.9 \text{ eV}$ , respectively.<sup>42</sup> The broadness of the Ir 4f peak indicates the deviation of  $\text{IrO}_2$  from standard rutile structure in both cases, and the asymmetry in both Ir 4f core-level peaks arise from conduction electrons screening both Ir 4f and O 1s core-holes.<sup>43-44</sup>

Given the absence of chemical differences, the morphologies of the two types of films were examined. The surface topographies of  $\text{IrO}_2/\text{Au}/\text{p}^+\text{-Si}$  and  $\text{IrO}_2/\text{Ir}/\text{p}^+\text{-Si}$ , determined via atomic force microscopy (AFM), are shown in Figure 1(c) and (d), respectively. These measurements reveal a much rougher surface of  $\text{IrO}_2/\text{Au}/\text{p}^+\text{-Si}$  than  $\text{IrO}_2/\text{Ir}/\text{p}^+\text{-Si}$ , with rms surface roughness values of  $1.6 \text{ nm}$  and  $0.4 \text{ nm}$ , respectively. AFM characterization of the samples prior to  $\text{IrO}_x$  deposition reveals that this is a consequence of a rougher  $\text{Au}/\text{p}^+\text{-Si}$  interface layer, which is characterized by a nanoparticulate morphology, likely as a consequence of dewetting due to direct deposition on the Si substrate (Figure S1). In contrast, the Ir layer on Si is extremely smooth (Figure S1). Consequently, it is likely that the increased surface area and thus increased concentration of active sites per geometric area could lead to a higher activity.

## 2. (Photo)electrochemical study on $\text{IrO}_2/\text{Au}/\text{p}^+(\text{n})\text{-Si}$ with different $\text{IrO}_2$ thicknesses

We further investigated the effect of thicknesses of  $\text{IrO}_2$  layer on the CV performance, aiming to obtain an optimum thickness for subsequent XAS studies. Three different thicknesses of  $\text{IrO}_x$  on  $\text{Au}/\text{p}^+\text{-Si}$  and  $\text{Au}/\text{p}^+\text{-Si}$  were prepared by controlling the sputtering time to achieve films of  $1 \text{ nm}$ ,  $2 \text{ nm}$ , and  $3 \text{ nm}$  thickness.

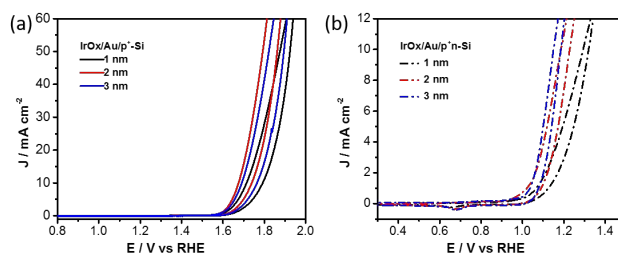


Figure 2. Cyclic voltammogram of  $\text{IrO}_x$  with different thicknesses ( $1 \text{ nm}$ ,  $2 \text{ nm}$ , and  $3 \text{ nm}$ ) on  $\text{Au}/\text{p}^+\text{-Si}$  (a) in the dark and  $\text{Au}/\text{p}^+\text{-Si}$  (b) under AM1.5 solar simulator irradiation in  $1 \text{ M H}_2\text{SO}_4$  aqueous solution measured at a scan rate of  $100 \text{ mV s}^{-1}$ .

Figure 2 shows cyclic voltammograms (CVs) of  $\text{IrO}_2$  with thicknesses of  $1$ ,  $2$ , and  $3 \text{ nm}$  on  $\text{p}^+\text{-Si}$  in the dark and on

p<sup>+</sup>n-Si under 100 mW cm<sup>-2</sup> irradiation in 1 M H<sub>2</sub>SO<sub>4</sub>. The dark anodes and illuminated photoanodes show an electrochemical oxidation pre-feature at ~1.3 V vs. RHE and ~0.8 V vs. RHE, respectively, followed by the steep onset of OER current. The precatalytic region was enlarged and shown in Figure S8. The electrochemical features in the pre-catalytic region are related to oxidation/reduction and/or charging of IrO<sub>x</sub>, though the assignment of chemical state transformation during those periods is still unclear and controversial.<sup>23, 45-46</sup> It was proposed that these features are related to a sort of “pre-rutile” structure, which is a non-interacting octahedral structure.<sup>23</sup> The redox current and OER current on the thinnest sample, i.e., 1 nm, are slightly lower compared to those on the 2 nm thick sample, but further increase of the thickness of IrO<sub>2</sub> to 3 nm had little additional impact on the CV characteristics. This trend is significantly different from the previous report on the IrO<sub>x</sub>/Ir/p<sup>+</sup>n-Si, where 2 nm IrO<sub>x</sub> showed much lower initial activity than the 4 and 6 nm ones.<sup>9</sup> This is likely a consequence of the high surface area of the catalyst on Au, which provides a larger concentration of active sites, even for thinner layers. Next, we will compare the *operando* XAS experiment on these samples under illumination and in the dark.

### 3. Operando XAS investigation of the ultrathin IrO<sub>2</sub>(1 nm)/Au/p<sup>+</sup>n-Si under light illumination and IrO<sub>2</sub>(1 nm)/Au/p<sup>+</sup>n-Si in the dark

Investigation of the ultrathin IrO<sub>2</sub> catalyst layers was performed under real PEC/EC OER conditions using the experimental setup shown schematically in Figure 3(a). The PEC cell was based on a three-electrode configuration in which the sample under investigation was used as the working electrode (WE), a Pt wire was used as the counter electrode (CE), and a Ag/AgCl electrode was used as the reference electrode. The WE was placed ~2 mm above the opening of the H-cell to form a hanging electrolyte meniscus. A 100 W heatless Xenon light source (LAX-C100, Asahi Spectra, USA) was used to illuminate the samples for PEC measurements. This configuration enabled study of the *operando* catalyst transformation as a function of the applied electrochemical potential.

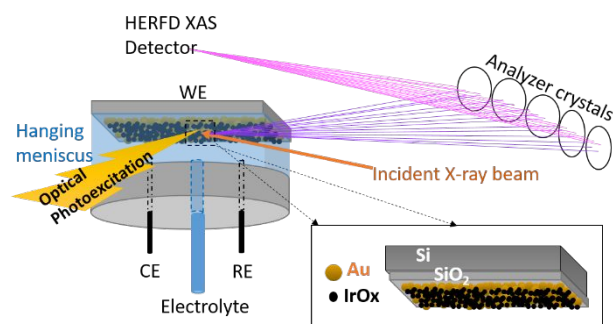


Figure 3. Schematic diagram of the *operando* (photo)electrochemical HERFD XAS experimental setup and the model of a photoelectrode.

A typical XAS spectrum is shown in Figure S2, where the most striking characteristic is a sharp and intense peak,

which is referred to as the white-line and arises from Ir2p→5d electronic transitions. Therefore, the white-line provides direct information about the Ir 5d unoccupied density of states. The energy position of the white-line indicates the oxidation state of Ir, which shifts by approximately +1.5 eV for each additional 5d hole, for example, when the oxidation state changes from Ir(III) (5d<sup>6</sup>) to Ir(IV) (5d<sup>5</sup>).<sup>47</sup> Thus, in the present work, we primarily focus on analyzing the change of the white-line as a function of applied electrochemical potential and illumination condition in order to characterize transformations of the IrO<sub>x</sub> catalyst that occur as it moves from the resting to active state.

X-ray absorption spectra obtained from the as-deposited catalyst in a dry environment are compared with the immersed catalyst at the open circuit potential (OCP) and the reference samples of K<sub>3</sub>IrCl<sub>6</sub> and IrO<sub>2</sub> (Figure S3). Upon exposure of the catalyst layer to the aqueous electrolyte, we observed a shift of the white line position to lower energies. To estimate the average oxidation states of IrO<sub>x</sub>, the white-line positions of the spectra are extracted by fitting the center of the spectra using a Gaussian peak function. The reference samples of K<sub>3</sub>IrCl<sub>6</sub> to IrO<sub>2</sub> give the peak positions of 11217.14 ± 0.01 eV and 11218.63 ± 0.02 eV, which correspond to Ir(III) and Ir(IV), respectively. This reference measurement is in agreement with the previous studies and confirms the expectation of a 1.5 eV shift per oxidation state for Ir(III) and Ir(IV).<sup>15, 23, 46, 48-51</sup> A linear relationship between the white line positions and valence state change are used to obtain the average oxidation states of IrO<sub>x</sub>.<sup>15, 23, 46, 48-51</sup> Using the same linear relationship, we estimate the average oxidation states of Ir in IrO<sub>x</sub> to be 3.98 and 3.43 for the dry and wet conditions, respectively. This suggests that partial reduction of IrO<sub>x</sub> from Ir(IV) to Ir(III) occurs under the OCP conditions, leading to the formation of an oxyhydroxide in the fashion of IrO(OH). This suggests that exposure of IrO<sub>2</sub> to the aqueous electrolyte leads to partial reduction of IrO<sub>x</sub> from Ir(IV) to Ir(III). The effect of the aqueous electrolyte could be understood by the formation of an oxyhydroxide in the fashion of IrO(OH).<sup>52-53</sup>

After evaluating the transformation of the catalyst layer upon solid/liquid interface formation at the OCP, we measured XAS of all the samples over a range of potentials, including a potential well below the water oxidation potential, at potentials below and above the redox potential commonly assigned to the Ir(III)/Ir(IV) transition, and to a potential at which significant oxygen evolution occurs, which is referred to as the *operando* condition.

Considering that Ir L<sub>III</sub> XAS is a “bulk” sensitive hard X-ray probe that provides average information of the whole film, three thicknesses of IrO<sub>x</sub> film (3 nm, 2 nm, and 1 nm) were examined in order to extract information related to surface transformations during catalysis. These three thickness offer different surface to bulk ratios; the 1 nm IrO<sub>x</sub> film provides a higher surface to bulk ratio than the 2 nm and 3 nm IrO<sub>x</sub> films. These IrO<sub>x</sub> films on Au/p<sup>+</sup>n-Si in the dark and Au/p<sup>+</sup>n-Si under irradiation were examined



by *operando* HERFD XAS at a series of potentials. The normalized XAS data are shown in Figure S4. All spectra in Figure S4 show the presence of strong white-line features indicating that there is a large local density of unoccupied 5d states at all potentials.<sup>23</sup> For both the dark electrode Au/p<sup>+</sup>-Si and photoanode Au/p<sup>+</sup>n-Si, the energy positions of the white-line gradually shift towards higher energies as the potential increased up to OER conditions. Such a shift

indicates an increase in the Ir oxidation state, which is in qualitative agreement with previous reports using conventional XAS.<sup>24</sup> The average oxidation states of Ir at different potentials were estimated based on the linear relationship between white line positions and Ir oxidation states (Figure S5 in SI).

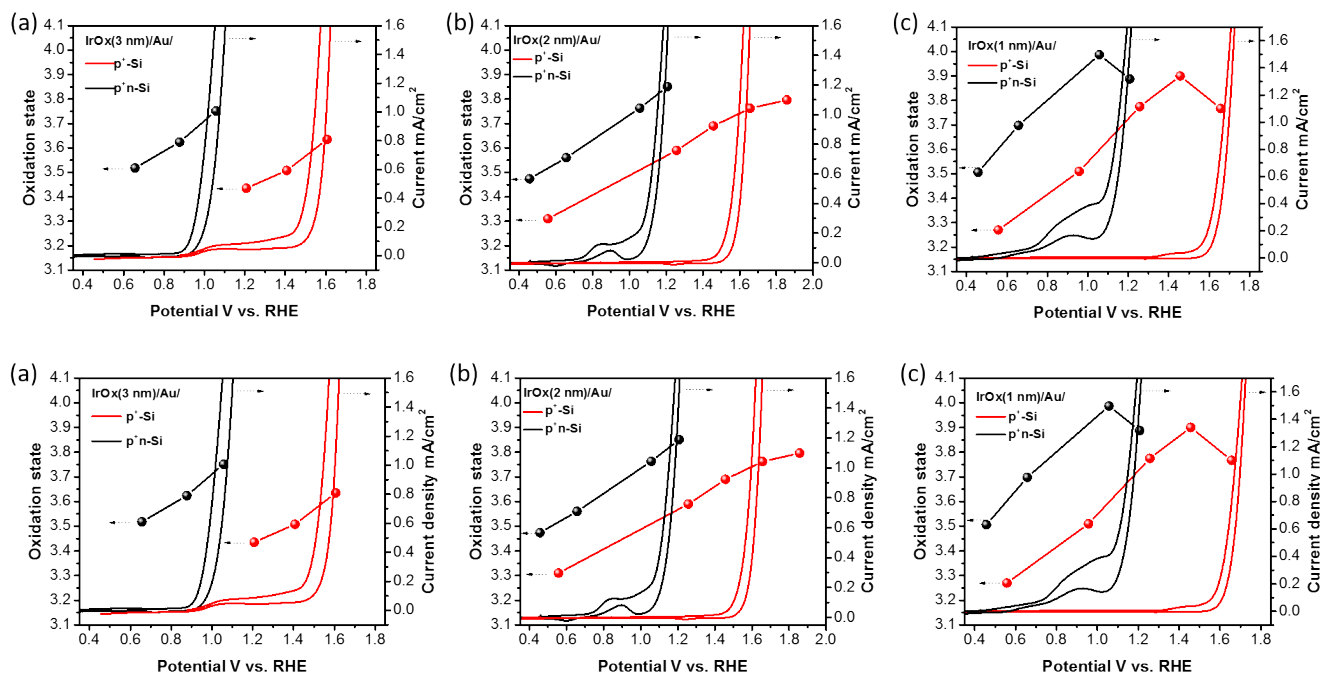


Figure 4. Cyclic voltammetry (right axis) recorded at 100 mV s<sup>-1</sup> in aqueous 1M H<sub>2</sub>SO<sub>4</sub> and corresponding Ir oxidation state (left axes) on IrO<sub>x</sub>/Au/p<sup>+</sup>-Si (red line) and IrO<sub>x</sub>/Au/p<sup>+</sup>n-Si (black line) as a function of applied potential. The thickness of IrO<sub>x</sub> is 3 nm (a), 2 nm (b), and 1 nm (c).

The average oxidation states of Ir at different potentials, together with corresponding CVs on IrO<sub>x</sub>/Au/p<sup>+</sup>-Si (red line) and IrO<sub>x</sub>/Au/p<sup>+</sup>n-Si (black line), are shown in Figure 4. For the 3 nm thick IrO<sub>x</sub> in Figure 4 (a), the average oxidation state of Ir on the photoanode p<sup>+</sup>n-Si (black dot) increased in parallel with that of dark anode p<sup>+</sup>-Si (red dot) as a function of applied potential. The difference of the potentials between the photoanode and dark anode are due to the photovoltage generated ~~in the former~~ under illumination. This trend of the average oxidation state with increasing voltage is similar to thinner IrO<sub>x</sub> films of 2 nm Figure 4 (b). Though they exhibit a similar trend, the shifts for 2 nm thick films are more pronounced than for 3 nm thick films (Figure S4 (a-d)). These pronounced shifts suggest larger changes in average oxidation states for 2 nm compared to 3 nm IrO<sub>x</sub> films (Figure 4(a & b)). For example, the average oxidation states reaches 3.76 and 3.86 at pre-OER and OER potentials, respectively, respectively on for the 2 nm electrode, while the corresponding average oxidation states for the 3 nm dark electrode are 3.62 and 3.74 at pre-OER and OER potentials, respectively. We further reduced the thickness of IrO<sub>x</sub> to 1 nm, shown in Figure 4 (c). As the potential is increased from 0.56 to 1.46 V vs. RHE for the dark electrode, the average oxidation

state gradually increases, and reaches the maximum at the potential after the pre-catalytic Ir oxidation peak and right before OER occurs (red dots in Figure 4 (c)). The trend of the average oxidation state with increasing voltage is similar to thicker IrO<sub>x</sub> films of 2 nm and 3 nm. However, it is worth noting the shifts for 1 nm thick films are more pronounced than for 2 nm and 3 nm thick films. Importantly, the average oxidation state decreased upon further increase of the potential from 1.46 to 1.66 V vs. RHE, where OER vigorously occurs. This phenomenon is observed for both non-photoactive anodes (p<sup>+</sup>-Si) and photoactive anodes (p<sup>+</sup>n-Si). The reduction of Ir oxidation state in the OER region proves the free energy DFT calculations by Nørskov *et al.*<sup>54</sup> They proposed that the most stable intermediate just below the onset of OER is fully covered with atomic O(IrO<sub>x</sub>-O), giving Ir the highest average oxidation state. The increase of the potential above the onset of OER, results in the release of O<sub>2</sub> and produces empty sites, which lowers the average oxidation states of Ir, as shown we see in Figure 4 (c). The increase of the potential above the onset of OER, results in the release of O<sub>2</sub> and produces empty sites not coordinated to atomic O. This lower coverage of atomic O leads to lower average oxidation states of Ir, as

we see in Figure 4 (c). The shifting of oxidation states towards lower states has also been observed by XAS on electrodeposited  $\text{IrO}_x$  films, which are porous and thicker under EC,<sup>23</sup> but was not clearly observed on other  $\text{IrO}_x$  films.<sup>15, 46, 48-51</sup>

In addition to the change of the white line position at different electrochemical potentials, it is also found that the width of the white-line increases as the potential is increased in Figure S4 (e & f). This effect can be understood in terms of the co-existence of two or more species with different oxidation states and induced broadening arising from crystal field split transitions.<sup>23, 47</sup> The crystal field split transitions may be observed in the second derivative of the spectra, which is characterized by two negative peaks when the bandwidth of the Ir 5d states is smaller than the crystal field splitting.<sup>55</sup> These two negative peaks correspond to the transition from the Ir 2p levels to the split ( $t_{2g} + e_g$ ) 5d states.<sup>56</sup> The second derivatives of the spectra are shown in Figure S6. The single-peak with the presence of a shoulder in the second derivative spectra indicates that the broadening we observed in Figure S4 (e & f) cannot be attributed to crystal field splitting.<sup>23, 47</sup> In another words, the increase of the width of the spectra with potential is due to the two or more species with different oxidation states, i.e., Ir(III), Ir(IV) and Ir(V). The Ir(V) feature was

suggested to only exist at the topmost surface of  $\text{IrO}_2$  nanocrystals by our group using ambient pressure XPS (APXPS), which is surface-sensitive technique.<sup>17</sup> Moreover, interpretation of XAS at the Ir  $L_{III}$  edge has led to the suggestion that the transformation of Ir(V) exists on anodic iridium oxide films and electrodeposited iridium oxide films.<sup>13,57</sup> However, Ir(V) was not observed on sputtered films.<sup>15, 46, 48-51</sup> This could be due to the differences in the composition, phase or structure of the films. Materials could transform differently as a function of deposition method.<sup>58</sup> The anodic and electrodeposited films are usually heavily hydrated porous materials, where nearly all the Ir sites are accessible to electrolyte and likely to enable more facile transformation to higher oxidation states during the reaction. In contrast, sputtered films are dense and anhydrous, where only the Ir sites located at the surface are accessible to electrolyte, as compared to the dense and anhydrous films made by sputtering. Moreover, Ir(III) associated with  $\text{O}(1-)$  species instead of Ir(V) was proposed during OER, using XPS, XAS and theoretical calculations.<sup>36, 59</sup> In the present work, the  $\text{IrO}_2$  film with the highest degree of transformation is 1 nm thick, but

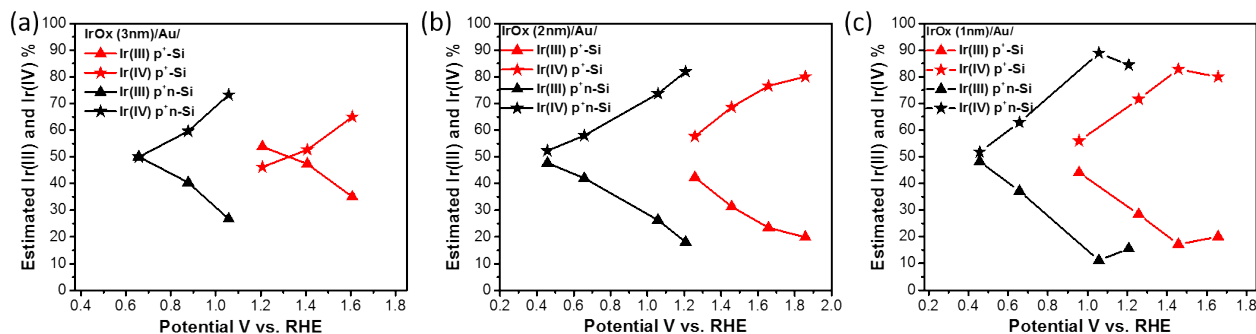


Figure 5. Estimated amount of Ir(III) (triangular) and Ir(IV) (star) as a function of applied potentials (a)  $\text{IrO}_x$  (3nm), (b)  $\text{IrO}_x$  (2nm) and (c)  $\text{IrO}_x$  (1nm) on Au/p<sup>+</sup>-Si (red line) and Au/p<sup>+</sup>n-Si (black line).

it is clear that Ir(V) is not the dominant component in the bulk materials during the catalytic process, as concluded from the average oxidation states discussed above.

Assuming the exclusive co-existence of Ir(III) and Ir(IV), the XAS spectra of Ir were fitted with a combination of an arctan step function and two Gaussian peaks with the fixed maxima positions at  $11217.14 \pm 0.01$  eV and  $11218.63 \pm 0.02$  eV, based on white lines of our Ir(III) and Ir(IV) references extracted from  $\text{K}_3\text{IrCl}_6$  and  $\text{IrO}_2$ , respectively. The proportion of the Ir(III) and Ir(IV) obtained from relative areas of the fitted Gaussian peaks are plotted as a function of applied potential (Figure 5).

The quantitative analysis based on fitting of XAS also shows that when the potential is increased from the pre-catalytic region to OER potentials, the concentration of Ir(IV) increases as the concentration of Ir(III) decreases in an almost linear way for both dark anodes (p<sup>+</sup>-Si) and

illuminated photoanodes (p<sup>+</sup>n-Si) for all the thicknesses, as shown in Figure 5 (a), (b), and (c). For instance, as seen in the Figure 5 (b), when the potential is increased from 0.58 to 1.46 V vs. RHE, the concentration of Ir(IV) increases while the concentration of Ir(III) decreases. Moreover, the dependences on potentials are nearly linear for both dark anodes (p<sup>+</sup>-Si) and illuminated photoanodes (p<sup>+</sup>n-Si) for all cases. With further increase of the potential to the OER region, the dependence on potential continues nearly linearly for both 3 nm and 2 nm  $\text{IrO}_x$ . However, for 1 nm  $\text{IrO}_x$  on p<sup>+</sup>-Si, further increase of the potential from 1.46 to 1.66 V vs. RHE, where OER occurs, leads to a slight decrease of Ir(IV) and slight increase of Ir(III). It is worth noting that the concentration of Ir(IV) remains above 80% for both photo and dark anodes in the OER region.

The difference of thicker films and ultra-thin films are interpreted in detail at below and above the OER onset potentials as follows.

First, the transformation below the onset of OER is much more significant on the 1 nm film. Comparing the photoanodes for example, at potentials just below onset of OER, i.e., 1.06 V vs RHE, the Ir(IV) on the 1 nm sample reaches a maximum of ~90%, while the value on the 2 nm and 3 nm samples are only about ~75%. This confirms that the catalytic transformation occurs on the surface rather than the bulk of the IrO<sub>x</sub>. For thicker films with lower electrolyte-accessible surface to volume ratio, the change is not as pronounced since a smaller fraction of the Ir atoms participate in catalytic reactions. This surface-limited transformation behavior confirms that our film is distinct from a “homogeneous” layer, which should yield a constant ratio of transformed Ir with changing film thickness, as seen in the electrodeposited layers.<sup>23</sup> However, our film is also not an absolutely dense layer, which should yield half the fractional Ir transformation with a doubling of the thicknesses, i.e., 45% vs. 90%. The origin of the disproportionate Ir redox activity can be understood by inspection of cross sectional TEM images (Figure S7). A film of ~4 nm IrO<sub>2</sub> layer on Au/Si shows that the IrO<sub>2</sub> layer consists of stacked 1–2 nm IrO<sub>2</sub> nanocrystals. On the 1 nm layer sample, the surface to bulk ratio is very high, resulting in transformation of 90% of the Ir atoms to Ir(IV). With increasing layer thickness to 2 nm, the nanocrystals are enlarged or stacked together, making the total surface area of nanocrystals larger than that of the 1 nm sample, but by less than a factor of two, so the ratio of surface of catalyst accessible to electrolyte to bulk materials is smaller.

Second, when the potential is swept above the onset potential of OER, the catalytic water oxidation by Ir(IV) is accompanied by the release of O<sub>2</sub> and leads to a reduction of Ir(IV) to Ir(III). At the same time, the oxidation of Ir(III) to Ir(IV) continues to occur. On the 1 nm sample with almost all of the Ir transformation to Ir(IV) (90%) below the onset potential, further oxidation is limited, so an average reduction of Ir(IV) to Ir(III) is observed. In contrast, the reduction of Ir at anodic potentials beyond the onset of OER is not observed for the case of the thicker films due to continuous oxidation of Ir(III) to Ir(IV) within the material. The oxidation of Ir(III) to Ir(IV) creates more active sites for water oxidation and the greater degree of Ir transformation on the 2 nm sample than on the 1 nm sample leads to a higher OER current (Figure 2). Further increase of film thickness from 2 nm to 3 nm does not improve the OER current further, likely since material deeper within the sample does not contribute to the reaction. Moreover, for a photoanode, where parasitic light absorption must be minimized, keeping the film as thin as possible is essential. Therefore, with a catalyst film with stacked nanocrystals, the optimal thickness for OER process in the sputtered films is balanced among the oxidation of water and catalyst itself, as well as kinetic release of O<sub>2</sub>. In our case, the optimal balance occurs at a thickness of approximately 2 nm.

## Conclusion

We developed an efficient IrO<sub>2</sub>/Au/p<sup>+</sup>n-Si photoanode operating in acidic solutions. The use of Au as the

interfacial layer results in lower onset potential, higher photocurrent, and higher photovoltage when compared to the reported Ir interfacial layer. The improvement could be related to the rougher surface of Au, as revealed by AFM and cross sectional TEM. The resulting IrO<sub>2</sub> thin film exhibited nanocrystals with the structurally labile surface and good coverage on Au with more exposed active sites, thereby leading to a superior photo and dark OER current. IrO<sub>2</sub> ultrathin films with controlled thicknesses were prepared by a sputtering process and the catalytic transformation properties were studied by *operando* HERFD XAS during OER under both EC and PEC conditions. On the ultrathin (1 nm) IrO<sub>2</sub> film, the average Ir oxidation state increases with increasing applied potential and reaches a 90% of transformation just below the OER onset potential. Above the onset potential, the ultrathin films show a decrease in oxidation state. This phenomenon is consistent with the free energy DFT calculations based on (110) surfaces of rutile-type IrO<sub>2</sub> proposed by Nørskov *et.al.*<sup>54</sup> Moreover, we show the first experimental evidence of reduced Ir at OER under realistic PEC conditions. When we increase the thicknesses of IrO<sub>2</sub>, the spectral changes become much less pronounced. This is due to the lower electrolyte-accessible surface to bulk ratio, where inner regions of the film are not accessible for the formation of hydroxide. This result further proves that the reaction is limited to the near-surface region of the IrO<sub>x</sub> film, which agrees with our earlier *operando* XPS study.<sup>17</sup> At potentials beyond the OER onset potential, the average oxidation state kept increasing on thicker films. By correlating the Ir oxidation state change results and OER performance (J-V) data, we can conclude the balancing properties that yield optimum thickness for PEC and EC performance. The XAS *operando* study provides important insight into observing the catalytic process and the optimum catalyst design compatible for sensitive photoanodes

## Supporting Information.

Experimental details, activity measurements, AFM, TEM, and *operando* HERFD-XAS measurements. This material is available free of charge via the Internet at <http://pubs.acs.org>.

## AUTHOR INFORMATION

### Corresponding Author

\* E-mail: [lin.li@kemi.uu.se](mailto:lin.li@kemi.uu.se), [sharp@wsi.tum.de](mailto:sharp@wsi.tum.de), [nilsson@slac.stanford.edu](mailto:nilsson@slac.stanford.edu)

### Present Addresses

†Anders Nilsson's current address is Fysikum, stockholm university, 106 91 Stockholm, Sweden

### Author Contributions

The manuscript was written through contributions of all authors. / All authors have given approval to the final version of the manuscript. / ‡ Lin Li and Jinhui Yang contributed equally to this work

## ACKNOWLEDGMENT

This material is based upon work performed by the Joint Center for Artificial Photosynthesis, a DOE Energy Innovation

Hub, supported through the Office of Science of the U.S. Department of Energy under Award Number DE-SC0004993. This research was partly carried out at the Stanford Synchrotron Radiation Light source, a National User Facility operated by Stanford University on behalf of the U.S. Department of Energy, Office of Basic Energy Sciences. H. A.-L. is supported by the Finnish Cultural Foundation and the KAUTE Foundation. L. L. is supported by the Wallenberg Foundation postdoctoral scholarship program "The MAX IV synchrotron radiation facility program" (KAW 2012.0359). We acknowledge Daniel Friebe and Anders F. Pedersen for the helpful discussions.

## ABBREVIATIONS

OER, oxygen evolution reaction; HERFD XAS, high energy resolution fluorescence detection X-ray absorption spectroscopy; PEC, photoelectrochemical; CV, cyclic voltammograms;

## REFERENCES

- (1). Lewis, N. S.; Nocera, D. G., Powering the planet: Chemical challenges in solar energy utilization. *Proc. Natl. Acad. Sci. U.S.A.* **2006**, *103*, 15729-15735.
- (2). Navarro Yerga, R. M.; Álvarez Galván, M. C.; del Valle, F.; Villoria de la Mano, J. A.; Fierro, J. L. G., Water Splitting on Semiconductor Catalysts under Visible-Light Irradiation. *ChemSusChem* **2009**, *2*, 471-485.
- (3). Chen, Y. W.; Prange, J. D.; Dühnen, S.; Park, Y.; Gunji, M.; Chidsey, C. E. D.; McIntyre, P. C., Atomic layer-deposited tunnel oxide stabilizes silicon photoanodes for water oxidation. *Nat. Mater.* **2011**, *10*, 539-544.
- (4). Yang, J.; Walczak, K.; Anzenberg, E.; Toma, F. M.; Yuan, G.; Beeman, J.; Schwartzberg, A.; Lin, Y.; Hettick, M.; Javey, A.; Ager, J. W.; Yano, J.; Frei, H.; Sharp, I. D., Efficient and Sustained Photoelectrochemical Water Oxidation by Cobalt Oxide/Silicon Photoanodes with Nanotextured Interfaces. *J. Am. Chem. Soc.* **2014**, *136*, 6191-6194.
- (5). Yang, J.; Cooper, J. K.; Toma, F. M.; Walczak, K. A.; Favaro, M.; Beeman, J. W.; Hess, L. H.; Wang, C.; Zhu, C.; Gul, S.; Yano, J.; Kisielowski, C.; Schwartzberg, A.; Sharp, I. D., A multifunctional biphasic water splitting catalyst tailored for integration with high-performance semiconductor photoanodes. *Nat. Mater.* **2017**, *16*, 335-341.
- (6). Hu, S.; Shaner, M. R.; Beardslee, J. A.; Lichterman, M.; Brunschwig, B. S.; Lewis, N. S., Amorphous TiO<sub>2</sub> coatings stabilize Si, GaAs, and GaP photoanodes for efficient water oxidation. *Science* **2014**, *344*, 1005-1009.
- (7). Tilley, S. D.; Cornuz, M.; Sivula, K.; Grätzel, M., Light-Induced Water Splitting with Hematite: Improved Nanostructure and Iridium Oxide Catalysis. *Angew. Chem. Int. Ed.* **2010**, *49*, 6405-6408.
- (8). Kenney, M. J.; Gong, M.; Li, Y.; Wu, J. Z.; Feng, J.; Lanza, M.; Dai, H., High-Performance Silicon Photoanodes Passivated with Ultrathin Nickel Films for Water Oxidation. *Science* **2013**, *342*, 836-840.
- (9). Mei, B.; Seger, B.; Pedersen, T.; Malizia, M.; Hansen, O.; Chorkendorff, I.; Vesborg, P. C. K., Protection of p+-n-Si Photoanodes by Sputter-Deposited Ir/IrO<sub>x</sub> Thin Films. *J. Phys. Chem. Lett.* **2014**, *5*, 1948-1952.
- (10). Lichterman, M. F.; Sun, K.; Hu, S.; Zhou, X.; McDowell, M. T.; Shaner, M. R.; Richter, M. H.; Crumlin, E. J.; Carim, A. I.; Saadi, F. H.; Brunschwig, B. S.; Lewis, N. S., Protection of inorganic semiconductors for sustained, efficient photoelectrochemical water oxidation. *Catal. Today* **2016**, *262*, 11-23.
- (11). Hu, S.; Lewis, N. S.; Ager, J. W.; Yang, J.; McKone, J. R.; Strandwitz, N. C., Thin-Film Materials for the Protection of Semiconducting Photoelectrodes in Solar-Fuel Generators. *J. Phys. Chem. C* **2015**, *119*, 24201-24228.
- (12). McCrory, C. C. L.; Jung, S.; Peters, J. C.; Jaramillo, T. F., Benchmarking Heterogeneous Electrocatalysts for the Oxygen Evolution Reaction. *J. Am. Chem. Soc.* **2013**, *135*, 16977-16987.
- (13). Danilovic, N.; Subbaraman, R.; Chang, K.-C.; Chang, S. H.; Kang, Y. J.; Snyder, J.; Paulikas, A. P.; Strmcnik, D.; Kim, Y.-T.; Myers, D.; Stamenkovic, V. R.; Markovic, N. M., Activity-Stability Trends for the Oxygen Evolution Reaction on Monometallic Oxides in Acidic Environments. *J. Phys. Chem. Lett.* **2014**, *5*, 2474-2478.
- (14). Danilovic, N.; Subbaraman, R.; Chang, K. C.; Chang, S. H.; Kang, Y.; Snyder, J.; Paulikas, A. P.; Strmcnik, D.; Kim, Y. T.; Myers, D.; Stamenkovic, V. R.; Markovic, N. M., Using Surface Segregation To Design Stable Ru-Ir Oxides for the Oxygen Evolution Reaction in Acidic Environments. *Angew. Chem. Int. Ed.* **2014**, *53*, 14016-14021.
- (15). Hüppauff, M.; Lengeler, B., Valency and Structure of Iridium in Anodic Iridium Oxide Films. *J. Electrochem. Soc.* **1993**, *140*, 598-602.
- (16). da Silva, G. C.; Perini, N.; Ticianelli, E. A., Effect of temperature on the activities and stabilities of hydrothermally prepared IrO<sub>x</sub> nanocatalyst layers for the oxygen evolution reaction. *Appl. Catal., B* **2017**, *218*, 287-297.
- (17). Sanchez Casalongue, H. G.; Ng, M. L.; Kaya, S.; Friebe, D.; Ogasawara, H.; Nilsson, A., In Situ Observation of Surface Species on Iridium Oxide Nanoparticles during the Oxygen Evolution Reaction. *Angew. Chem. Int. Ed.* **2014**, *53*, 7169-7172.
- (18). Kötze, R.; Barbero, C.; Haas, O., Probe beam deflection investigation of the charge storage reaction in anodic iridium and tungsten oxide films. *J. Electroanal. Chem.* **1990**, *296*, 37-49.
- (19). Willinger, E.; Massué, C.; Schlögl, R.; Willinger, M. G., Identifying Key Structural Features of IrO<sub>x</sub> Water Splitting Catalysts. *J. Am. Chem. Soc.* **2017**, *139*, 12093-12101.
- (20). Minguzzi, A.; Lugaesi, O.; Locatelli, C.; Rondinini, S.; D'Acapito, F.; Achilli, E.; Ghigna, P., Fixed Energy X-ray Absorption Voltammetry. *Anal. Chem.* **2013**, *85*, 7009-7013.
- (21). Lebedev, D.; Povia, M.; Waltar, K.; Abdala, P. M.; Castelli, I. E.; Fabbri, E.; Blanco, M. V.; Fedorov, A.; Copéret, C.; Marzari, N.; Schmidt, T. J., Highly Active and Stable Iridium Pyrochlores for Oxygen Evolution Reaction. *Chem. Mater.* **2017**, *29*, 5182-5191.
- (22). Hillman, A. R.; Skopek, M. A.; Gurman, S. J., X-Ray spectroscopy of electrochemically deposited iridium oxide films: detection of multiple sites through structural disorder. *Phys. Chem. Chem. Phys.* **2011**, *13*, 5252.
- (23). Minguzzi, A.; Lugaesi, O.; Achilli, E.; Locatelli, C.; Vertova, A.; Ghigna, P.; Rondinini, S., Observing the oxidation state turnover in heterogeneous iridium-based water oxidation catalysts. *Chem. Sci.* **2014**, *5*, 3591.
- (24). Pauporté, T.; Aberdam, D.; Hazemann, J.-L.; Faure, R.; Durand, R., X-ray absorption in relation to valency of iridium in sputtered iridium oxide films. *J. Electroanal. Chem.* **1999**, *465*, 88-95.
- (25). Singh, J.; Lamberti, C.; Bokhoven, J. A. v., Advanced X-ray absorption and emission spectroscopy: in situ catalytic studies. *Chem. Soc. Rev.* **2010**, *39*, 4754-4766.
- (26). Trotochaud, L.; Mills, T. J.; Boettcher, S. W., An Optocatalytic Model for Semiconductor-Catalyst Water-Splitting Photoelectrodes Based on In Situ Optical Measurements on Operational Catalysts. *J. Phys. Chem. Lett.* **2013**, *4*, 931-935.



- (27). Baran, T.; Fracchia, M.; Vertova, A.; Achilli, E.; Naldoni, A.; Malara, F.; Rossi, G.; Rondinini, S.; Ghigna, P.; Minguzzi, A.; D'Acapito, F., Operando and Time-Resolved X-Ray Absorption Spectroscopy for the Study of Photoelectrode Architectures. *Electrochim. Acta* **2016**, *207*, 16-21.
- (28). Yoshida, M.; Yomogida, T.; Mineo, T.; Nitta, K.; Kato, K.; Masuda, T.; Nitani, H.; Abe, H.; Takakusagi, S.; Uruga, T.; Asakura, K.; Uosaki, K.; Kondoh, H., In situ observation of carrier transfer in the Mn-oxide/Nb:SrTiO<sub>3</sub> photoelectrode by X-ray absorption spectroscopy. *Chem. Commun.* **2013**, *49*, 7848-7850.
- (29). Yoshida, M.; Yomogida, T.; Mineo, T.; Nitta, K.; Kato, K.; Masuda, T.; Nitani, H.; Abe, H.; Takakusagi, S.; Uruga, T.; Asakura, K.; Uosaki, K.; Kondoh, H., Photoexcited Hole Transfer to a MnOx Cocatalyst on a SrTiO<sub>3</sub> Photoelectrode during Oxygen Evolution Studied by In Situ X-ray Absorption Spectroscopy. *J. Phys. Chem. C* **2014**, *118*, 24302-24309.
- (30). Kurosu, H.; Yoshida, M.; Mitsutomi, Y.; Onishi, S.; Abe, H.; Kondoh, H., In Situ Observations of Oxygen Evolution Cocatalysts on Photoelectrodes by X-ray Absorption Spectroscopy: Comparison between Cobalt-Phosphate and Cobalt-Borate. *Electrochemistry* **2016**, *84*, 779-783.
- (31). Minguzzi, A.; Naldoni, A.; Lugaresi, O.; Achilli, E.; D'Acapito, F.; Malara, F.; Locatelli, C.; Vertova, A.; Rondinini, S.; Ghigna, P., Observation of charge transfer cascades in  $\alpha$ -Fe<sub>2</sub>O<sub>3</sub>/IrOx photoanodes by operando X-ray absorption spectroscopy. *Phys. Chem. Chem. Phys.* **2017**, *19*, 5715-5720.
- (32). Eisenberger, P.; Platzman, P. M.; Winick, H., X-Ray Resonant Raman Scattering: Observation of Characteristic Radiation Narrower than the Lifetime Width. *Phys. Rev. Lett.* **1976**, *36*, 623-626.
- (33). Friebe, D.; Mbuga, F.; Rajasekaran, S.; Miller, D. J.; Ogasawara, H.; Alonso-Mori, R.; Sokaras, D.; Nordlund, D.; Weng, T.-C.; Nilsson, A., Structure, Redox Chemistry, and Interfacial Alloy Formation in Monolayer and Multilayer Cu/Au(111) Model Catalysts for CO<sub>2</sub> Electroreduction. *J. Phys. Chem. C* **2014**, *118*, 7954-7961.
- (34). Friebe, D.; Miller, D. J.; O'Grady, C. P.; Anniyev, T.; Bargar, J.; Bergmann, U.; Ogasawara, H.; Wikfeldt, K. T.; Pettersson, L. G. M.; Nilsson, A., In situ X-ray probing reveals fingerprints of surface platinum oxide. *Phys. Chem. Chem. Phys.* **2010**, *13*, 262-266.
- (35). Friebe, D.; Miller, D. J.; Nordlund, D.; Ogasawara, H.; Nilsson, A., Degradation of Bimetallic Model Electrocatalysts: An In Situ X-Ray Absorption Spectroscopy Study. *Angew. Chem. Int. Ed.* **2011**, *50*, 10190-10192.
- (36). Friebe, D.; Viswanathan, V.; Miller, D. J.; Anniyev, T.; Ogasawara, H.; Larsen, A. H.; O'Grady, C. P.; Nørskov, J. K.; Nilsson, A., Balance of Nanostructure and Bimetallic Interactions in Pt Model Fuel Cell Catalysts: In Situ XAS and DFT Study. *J. Am. Chem. Soc.* **2012**, *134*, 9664-9671.
- (37). Merte, L. R.; Beharfarid, F.; Miller, D. J.; Friebe, D.; Cho, S.; Mbuga, F.; Sokaras, D.; Alonso-Mori, R.; Weng, T.-C.; Nordlund, D.; Nilsson, A.; Roldan Cuenya, B., Electrochemical Oxidation of Size-Selected Pt Nanoparticles Studied Using in Situ High-Energy-Resolution X-ray Absorption Spectroscopy. *ACS Catal.* **2012**, *2*, 2371-2376.
- (38). Friebe, D.; Bajdich, M.; Yeo, B. S.; Louie, M. W.; Miller, D. J.; Casalongue, H. S.; Mbuga, F.; Weng, T.-C.; Nordlund, D.; Sokaras, D.; Alonso-Mori, R.; Bell, A. T.; Nilsson, A., On the chemical state of Co oxide electrocatalysts during alkaline water splitting. *Phys. Chem. Chem. Phys.* **2013**, *15*, 17460-17467.
- (39). Friebe, D.; Louie, M. W.; Bajdich, M.; Sanwald, K. E.; Cai, Y.; Wise, A. M.; Cheng, M.-J.; Sokaras, D.; Weng, T.-C.; Alonso-Mori, R.; Davis, R. C.; Bargar, J. R.; Nørskov, J. K.; Nilsson, A.; Bell, A. T., Identification of Highly Active Fe Sites in (Ni,Fe)OOH for Electrocatalytic Water Splitting. *J. Am. Chem. Soc.* **2015**, *137*, 1305-1313.
- (40). Andreas, H.; Elzanowska, H.; Serebrennikova, I.; Birss, V., Hydrous Ir Oxide Film Properties at Sol - Gel Derived Ir Nanoparticles. *J. Electrochem. Soc.* **2000**, *147*, 4598-4604.
- (41). Gorlin, Y.; Chung, C.-J.; Benck, J. D.; Nordlund, D.; Seitz, L.; Weng, T.-C.; Sokaras, D.; Clemens, B. M.; Jaramillo, T. F., Understanding Interactions between Manganese Oxide and Gold That Lead to Enhanced Activity for Electrocatalytic Water Oxidation. *J. Am. Chem. Soc.* **2014**, *136*, 4920-4926.
- (42). A. V. Naumkin, A. K.-V., S. W. Garrenstroom, C. J. Powell, X-ray Photoelectron Spectroscopy Database XPS, Version 4.1, NIST Standard Reference Database 20. National Institute of Standards and Technology: 2012.
- (43). Pfeifer, V.; Jones, T. E.; Vélez, J. J. V.; Massué, C.; Arrigo, R.; Teschner, D.; Girgsdies, F.; Scherzer, M.; Greiner, M. T.; Allan, J.; Hashagen, M.; Weinberg, G.; Piccinin, S.; Hävecker, M.; Knop - Gericke, A.; Schlögl, R., The electronic structure of iridium and its oxides. *Surf. Interface Anal.* **2016**, *48*, 261-273.
- (44). Freakley, S. J.; Ruiz - Esquius, J.; Morgan, D. J., The X-ray photoelectron spectra of Ir, IrO<sub>2</sub> and IrCl<sub>3</sub> revisited. *Surf. Interface Anal.* **2017**, *49*, 794-799.
- (45). Steegstra, P.; Busch, M.; Panas, I.; Ahlberg, E., Revisiting the Redox Properties of Hydrous Iridium Oxide Films in the Context of Oxygen Evolution. *J. Phys. Chem. C* **2013**, *117*, 20975-20981.
- (46). Mo, Y.; Stefan, I. C.; Cai, W.-B.; Dong, J.; Carey, P.; Scherson, D. A., In Situ Iridium LIII-Edge X-ray Absorption and Surface Enhanced Raman Spectroscopy of Electrodeposited Iridium Oxide Films in Aqueous Electrolytes. *J. Phys. Chem. B* **2002**, *106*, 3681-3686.
- (47). Clancy, J. P.; Chen, N.; Kim, C. Y.; Chen, W. F.; Plumb, K. W.; Jeon, B. C.; Noh, T. W.; Kim, Y.-J., Spin-orbit coupling in iridium-based 5d compounds probed by x-ray absorption spectroscopy. *Phys. Rev. B* **2012**, *86*, 195131.
- (48). Pedersen, A. F.; Escudero-Escribano, M.; Sebok, B.; Bodin, A.; Paoli, E.; Frydendal, R.; Friebe, D.; Stephens, I. E. L.; Rossmel, J.; Chorkendorff, I.; Nilsson, A., Operando XAS Study of the Surface Oxidation State on a Monolayer IrOx on RuOx and Ru Oxide Based Nanoparticles for Oxygen Evolution in Acidic Media. *J. Phys. Chem. B* **2018**, *122*, 878-887.
- (49). Achilli, E.; Minguzzi, A.; Lugaresi, O.; Locatelli, C.; Rondinini, S.; Spinolo, G.; Ghigna, P., In Situ Dispersive EXAFS in Electrocatalysis: The Investigation of the Local Structure of IrOx in Chronoamperometric Conditions as a Case Study. *J. spectrosc.* **2014**, *480*102.
- (50). Pfeifer, V.; Jones, T. E.; Wrabetz, S.; Massué, C.; Vélez, J. J. V.; Arrigo, R.; Scherzer, M.; Piccinin, S.; Hävecker, M.; Knop-Gericke, A.; Schlögl, R., Reactive oxygen species in iridium-based OER catalysts. *Chem. Sci.* **2016**, *7*, 6791-6795.
- (51). Pfeifer, V.; Jones, T. E.; Vélez, J. J. V.; Massué, C.; Greiner, M. T.; Arrigo, R.; Teschner, D.; Girgsdies, F.; Scherzer, M.; Allan, J.; Hashagen, M.; Weinberg, G.; Piccinin, S.; Hävecker, M.; Knop-Gericke, A.; Schlögl, R., The electronic structure of iridium oxide electrodes active in water splitting. *Phys. Chem. Chem. Phys.* **2016**, *18*, 2292-2296.
- (52). Gauthier, J. A.; Dickens, C. F.; Chen, L. D.; Doyle, A. D.; Nørskov, J. K., Solvation Effects for Oxygen Evolution Reaction Catalysis on IrO<sub>2</sub>(110). *J. Phys. Chem. C* **2017**, *121*, 11455-11463.
- (53). Kötzt, R.; Neff, H.; Stucki, S., Anodic Iridium Oxide Films XPS - Studies of Oxidation State Changes and. *J. Electrochem. Soc.* **1984**, *131*, 72-77.

(54). Rossmeisl, J.; Qu, Z. W.; Zhu, H.; Kroes, G. J.; Nørskov, J. K., Electrolysis of water on oxide surfaces. *J. Electroanal. Chem.* **2007**, 607, 83-89.

(55). Choy, J.-H.; Kim, D.-K.; Hwang, S.-H.; Demazeau, G.; Jung, D.-Y., XANES and EXAFS Studies on the Ir-O Bond Covalency in Ionic Iridium Perovskites. *J. Am. Chem. Soc.* **1995**, 117, 8557-8566.

(56). Choy, J.-H.; Kim, D.-K.; Demazeau, G.; Jung, D.-Y., LIII-Edge XANES Study on Unusually High Valent Iridium in a Perovskite Lattice. *J. Phys. Chem.* **1994**, 98, 6258-6262.

(57). Minguzzi, A.; Locatelli, C.; Lugaresi, O.; Achilli, E.; Cappelletti, G.; Scavini, M.; Coduri, M.; Masala, P.; Sacchi, B.;

Vertova, A.; Ghigna, P.; Rondinini, S., Easy Accommodation of Different Oxidation States in Iridium Oxide Nanoparticles with Different Hydration Degree as Water Oxidation Electrocatalysts. *ACS Catal.* **2015**, 5, 5104-5115.

(58). Lin, F.; Boettcher, S. W., Adaptive semiconductor/electrocatalyst junctions in water-splitting photoanodes. *Nat. Mater.* **2014**, 13, 81-86.

(59). Pfeifer, V.; Jones, T. E.; Vélez, J. J. V.; Arrigo, R.; Piccinin, S.; Hävecker, M.; Knop-Gericke, A.; Schlögl, R., In situ observation of reactive oxygen species forming on oxygen-evolving iridium surfaces. *Chem. Sci.* **2017**, 8, 2143-2149.

## TOC

